The effect of ignition protocol on grassfire development

D. Sutherland *†‡, J.J. Sharples †‡, K.A.M Moinuddin §‡

September 13, 2019

Abstract

The effect of ignition protocol on the development of grassfires is investigated using physics-based simulation. Simulation allows measurement of the forward rate of spread of a fire as a function of time at high temporal resolution. Two ignition protocols are considered: the inward ignition protocol, where the ignition proceeds in a straight line from the edges of the burnable fire plot to the centre of the plot; and the outwards ignition protocol, where the ignition proceeds from the centre of the burnable fire plot to the edges of the plot. In addition to the two ignition protocols, the wind speed, time taken for the ignition to be completed, and the ignition line length are varied. The rate of spread (R) of the resultant fires is analysed. The outwards ignition protocol leads to a (roughly) monotonic increase in R, whereas the inward ignition protocol can lead to a peak in R before decreasing to the quasi-equilibrium R. The fires simulated here typically take 50 m from the ignition line to develop a quasi-equilibrium R. The results suggest that a faster ignition is preferable to achieve a quasi-equilibrium R in the shortest distance from the ignition line.

*Corresponding author; E duncan.sutherland@adfa.edu.au T +61 2 6268 8884

†School of Science, University of New South Wales, Canberra, PO Box 7916, Canberra BC, ACT 2610, Australia

‡Bushfire Natural Hazards Cooperative Research Centre, East Melbourne, Victoria, 3002, Australia

§Institute for Sustainable Industries and Livable Cities, Victoria University, Melbourne, Victoria, 8001, Australia

Introduction

Models for rate of fire spread are used extensively in the assessment of wildfire risk. In particular, they are used to assess the likely progression of a fire, which then informs decisions around resource allocation and community safety (e.g. evacuations). Currently, all of the operational rate of spread models used in Australia are empirically based, having drawn upon fire spread data collected through a variety of field-scale experimental programs dating back to the 1950s (Cruz *et al.*, 2015a).

Conducting field-scale fire experiments is both labour and cost intensive, involving many months of careful preparation and instrumentation of the experimental plots, conducting the actual experiments, and then analysing the resultant data. As an example, the Annaburroo experiments conducted in the Northern Territory by Cheney *et al.* (1993) involved a total of 170 plots ranging in size from 100 m $\times$100 m to 200 m $\times$300 m, with 121 of them burned and analysed (Cheney *et al.*, 1993). These experiments improved our understanding of the effect of wind speed, dead fuel moisture content and fire line width on rate of spread. Indeed, they underpin the current grassland fire spread model used operationally in Australia. Data from the Annaburroo experiments have also been used to evaluate the performance of physics-based fire spread simulators (Moinuddin *et al.*, 2018; Mell *et al.*, 2007).

One of the factors that must be considered in fire experiments is the manner in which the fires are initiated. This includes the method used to establish the fire line and the ultimate shape that it assumes – this is an important consideration because it is known that the overall shape of a fire can influence its observed rate of spread (Frangieh *et al.*, 2018). The ignition line length also influences the overall shape (Linn and Cunningham, 2005) and spread rate Canfield *et al.* (2014) of the fire. In the Annaburroo experiments the fire was ignited by two workers who started at the centre of the upwind edge of the burn plot. The workers then walked slowly in opposite directions with drip torches to ignite the fire. It took approximately one minute to establish the fire line. More recently, Cruz *et al.* (2015b) conducted a number of grassland fire experiments on 33 m $\times$33 m plots in Victoria and New South Wales, and adopted a different ignition protocol to that used by Cheney *et al.*. In these experiments, two workers with drip torches started at opposite corners of the upwind edge of the burn plot and quickly moved towards each other, joining the fire line at the centre of the burn plot (Cruz *et al.*, 2015b).

The ignition protocol adopted by Cruz *et al.* was chosen so that the experimental fire would develop to a quasi-equilibrium state more quickly (M.Cruz, pers. comm.). On this point, it is important to recognise that the primary aim of operational fire spread prediction systems is to predict the rate of spread of a fire once it has reached a quasi-equilibrium state. Hence, it is desirable that the fire attains this state for as long as possible during the experimental burn. However, regardless of the reason for choosing one ignition protocol over another, it is natural to question how differences in ignition protocol might affect the subsequent development of the fire. This question is particularly pertinent when existing empirical models are refined or updated based on new data obtained from experiments that may have used different ignition protocols to the original experiments. The impact of differing ignition protocols on an updated empirical model is difficult to estimate. If experimental data is taken from any quasi-equilibrium fire, then the data nominally will be consistent. However, the quasi-equilibrium state may be quite difficult to judge, especially from measurements at large time intervals. It is currently unclear how ignition protocol effects the development of the fire to its quasi-equilibrium rate of spread. In physics-based simulations, the fire location data is known at high temporal resolution and therefore it is easy to measure the development of R to quasi-equilibrium values.

This study seeks to answer the question: do different ignition protocols significantly affect the quasi-equilibrium rate of spread of the fire and the time taken for the fire to develop to a quasi-equilibrium state? Specifically, physics-based simulations of fires in grassland are used to investigate the differences in R resulting from different ignition protocols, while all other factors are kept the same.

Physics-based modelling

The physics based model Wild Fire Dynamics Simulator (WFDS 6.0.0, subversion 9977) was used for this study. WFDS solves the governing equations for low-Mach number buoyant flow using a finite difference scheme and radiative heat transfer using a finite volume method. The thermal degradation of vegetative fuel was modelled using a semi-empirical approach where the mass loss rate of the fuel was modelled by a linear equation fitted to data. A mixed-is-burned combustion model (McGrattan *et al.*, 2013) was used so that fuel gasses undergo the combustion reaction, and release heat, when the concentration of gasses in a computational grid cell exceeds the stoichiometric ratio for the combustion reaction. Turbulent processes are modelled using the principle of Large Eddy Simulation (LES). Large fluid structures are resolved explicitly but smaller sub-grid-scale turbulent processes are modelled. The combustion model and LES are discussed in detail by McGrattan *et al.* (2013) and McDermott *et al.* (2011).

The simulations presented here are an extension of Moinuddin *et al.* (2018). As such, the domain size, configuration, and grid resolutions used in the present study are identical to Moinuddin *et al.* (2018). The simulations were performed over a domain that is 960 m long, 640 m wide and 100 m high. The inlet wind velocity was prescribed as a 1/7th-power law model following previous efforts (Moinuddin *et al.*, 2018; Mell *et al.*, 2007; Morvan *et al.*, 2013) and the inlet wind speed U_2 was specified at 2 m above the ground. That is,

$$u_{in}(z) = U_2 \left(\frac{z}{2}\right)^{\frac{1}{7}} . \qquad (1)$$

Note there is no prescribed synthetic inlet turbulence. The long fetch before the burning domain allows the flow to develop naturally though the domain. There is a sudden change of surface properties, a smooth no-slip boundary transitions to grass modelled with an aerodynamic drag, at 20 m from the inlet. The sudden transition in surface roughness causes the flow to develop turbulence. Coincidentally, the inlet velocity U_2 is approximately the same as u_{10} over the fire ground. For the three inlet velocities the $u_{10} = 2.7$, 6.2, 10.7 m s^{-1}. The temperature is constant on all boundaries.

The simulation domain was composed of multiple subdomains. Adjacent to the inlet is a non-burning subdomain of length 660 m. The burnable grass plot, which has dimensions 104 m ×108 m to mimic the Annaburroo experiments (Cheney *et al.*, 1993), was placed downwind after the first subdomain. A non-burnable subdomain (approximately 200 m long) is placed downwind of the burnable plot and upwind of the open outlet boundary. Bordering subdomains (approximately 270 m wide) are placed on either side of the burnable plot. A schematic of the computational domain showing the location of the burn plot and the fine grid is shown in Figure 1.

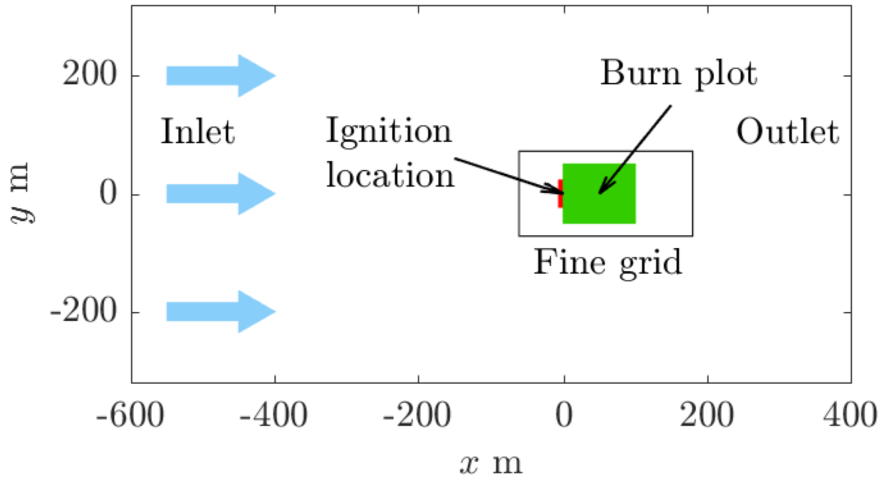

Figure 1: A plan view schematic of the computational domain. The burnable area is shown in green, and the fine 0.25 m ×0.25 m ×0.25 m grid is also depicted. The red line marks the location of the line ignitions used in the simulations. The blue arrows represent the applied driving wind.

Precursor simulations, conducted without burning, were used to ensure the atmospheric boundary layer above the grassland was well-developed. The flow was considered well-developed when only turbulent fluctuations were observed in the velocity profile over the burnable plot. To reduce computational spin-up time, the velocity fields obtained from the precursor simulations were used to initialise all the fire simulations.

Following Moinuddin *et al.* (2018) a grid resolution of 0.25 m in all directions was used over the burnable grass plot up to a height of 6 m above the grass surface. Coarser resolutions, again identical to those used by Moinuddin *et al.* (2018) were used in the non-burning subdomains. The fires considered here are of similar size and intensity to the fires studied by Moinuddin *et al.* (2018). It is important to ensure the simulation results are not influenced by the choice of grid resolution or domain size. Moinuddin *et al.* (2018) investigated multiple grid resolutions including stretched grids. Because stretched grids were found to not yield grid independent results we will discuss only uniform grid independence tests. Three grid sizes were considered: coarse 0.5 m resolution, medium 0.25 m resolution, and fine 0.167 m resolution. The frontal location and R_{qe} for the medium and fine resolution simulations were almost identical whereas, the coarse resolution gave a R_{qe} of approximately half the value for the medium and fine resolution grids. Therefore, the 0.25 m resolution was selected for these simulations. Moinuddin *et al.* (2018) also investigated three domain sizes. The domain sizes considered were: the small domain 640 m long $\times$ 440 m wide $\times$ 60 m height, the medium domain 960 m long $\times$ 640 m wide $\times$ 100 m height, and the large domain, 1320 m long $\times$ 760 m wide $\times$ 120 m height. The heat release rate, fire front location, and rate of spread for the medium and large domains were found to exhibit only minor differences, whereas the small and medium domain results exhibited differences of nearly 100% in magnitude. Therefore the medium domain was selected.

The lateral, top, and downwind boundaries are all open (constant pressure). The ground was a no-slip boundary imposed by a log-law of the wall. The fuel was modelled as a thin layer on the bottom boundary, under the assumption that for large fires most of heat released occurs above the fuel bed and so heat transfer within the fuel bed itself was predominantly in the vertical direction. A separate high-resolution grid was used within the fuel bed to resolve the vertical radiant heat transfer. The drag force of the grassland was modelled using a standard aerodynamic drag force term, using drag coefficient and leaf area index parameters the same as those used by Mell *et al.* (2007).

Following Morvan and Dupuy (2004) a linear model of thermal degradation of fuel was used in these simulations. The mass-loss-rate of the solid fuel degrading under heating is assumed to be linear and begins at a critical temperature of 400 K. The degradation of fuel terminates at 500 K. All the thermo-physical, pyrolysis and combustion parameters are identical to those used by Moinuddin *et al.* (2018) and were again selected to replicate the grassfire experiments of Cheney *et al.* (1993). Parameters such as vegetation height (0.21 m) and load (0.283 kg m^{-2}) were taken from Mell *et al.* (2007) whereas fuel and thermo-physical parameters; i.e. heat of combustion (16400 kJ kg^{-1}), heat of pyrolysis (200 kJ kg^{-1}), the vegetation char fraction is 0.17, and the soot yield (0.008 unitless), were chosen to match experimental measurements of cellulosic fuel. The vegetation moisture content was 0.063, the surface-to-volume ratio of vegetation was 9770 m^{-1}, the vegetation element density is 440 kg m^{-3}, and the drag coefficient is 0.125. The emissivity is 0.99 and the maximum mass loss rate is 0.15 kg s^{-1} m^{-3}. The ambient temperature is 305 K and relative humidity 40%. For further details on the selection of thermophysical, pyrolysis, and combustion parameters see Moinuddin *et al.* (2018).

Varying ignition protocol

The simulated grassfires were ignited along the upwind edge of the burn plot by applying a prescribed heat release rate (HRR) per unit area of 750 kW m^{-2} for a duration of 4 seconds. The ignition line had a constant width of 2 m, a total length of L_i, and is discretised into eight sections (except for the largest L_i cases where 16 sections were used) of equal length ℓ. To emulate the movement of the ignition crews in the experiments of Cheney *et al.* (1993) and Cruz *et al.* (2015b), different sections were ignited at different times. In particular, two different models of the ignition process were considered: an inward ignition protocol and an outward ignition protocol.

For the inward ignition protocol, the outermost sections of the upwind edge were ignited first. The next innermost sections were then ignited successively in time steps of $\delta t_i = \ell/u_i$, where u_i is the ignition speed - faster ignition speeds correspond to faster moving workers with drip torches. The outward ignition protocol was modelled in a similar manner, but with the innermost sections ignited first and the next outermost sections successively ignited in time steps of δt_i. In this study three ignition speeds were considered: $u_i = 0.5, 1.0$ and 2.4 m s^{-1}, for each of ignition protocols.

To demonstrate the differences in the ignition protocols, fire line contours (for the $U_2 = 6$ m s^{-1}, $u_i = 1.0$ m s^{-1} and $L_i = 48$ m case) during the ignition process are shown in Figure 2.

The isochrones of the simulated fires were obtained by examining the bottom boundary temperature. Under the linear thermal degradation model used in WFDS, pyrolysis of the solid fuel occurs when the temperature T of the solid fuel, i.e. the bottom boundary, exceeds 400 K. Due to the nature of the ignition protocols, it takes some time before a single continuous fire line is established. As a consequence, the time of ignition is slightly difficult to interpret. In Figure 2, time is measured from when ignition commences, either at the outer edges for the inward protocol, or at the centre of the plot for the outward protocol. Initially, the inward ignition fire (Fig. 2b) lags slightly behind the outward ignition fire (Fig. 2a), but ultimately overtakes it. Over the entire simulation period shown in Figure 2, the inward ignition fire spreads about 12% further than the outward ignition fire. To clarify the three-dimensional shapes of the two fires (U6u1L48i and U6u1L48o), two renderings of the flame and soot mass fraction are shown in Figure 3. These images were made using the WFDS companion program Smokeview (Forney, 2019). The flame was visualised using the 80 kW m^{-3} isosurface of heat release rate per unit volume. The fires are both shown at 21 s after the ignition process commences. The smoke plume of the inward ignition fire is more vertical than the smoke plume of the outward ignition fire, suggesting that the inward ignition fire is more intense at that point in time.

Parameter space

All simulations were performed with both the inward and outward protocols. The effect of ignition line speed u_i, inlet wind speed U_2, and ignition line length L_i were all investigated independently.

Inlet wind speeds of $U_2 = 3, 6, 10$ m s^{-1} were considered. The varying wind speed simulations were performed with $u_i = 1.0$ m s^{-1} and $L_i = 48$ m.

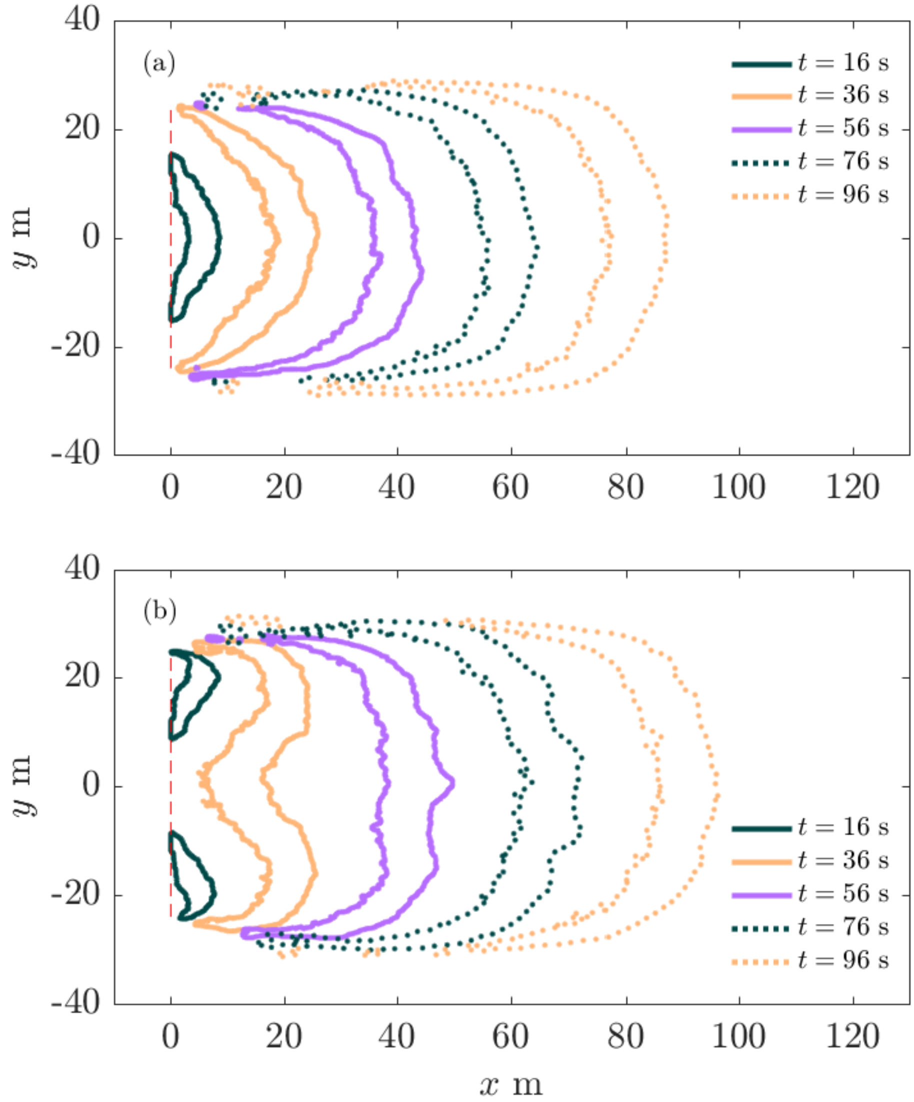

Figure 2: The simulated isochrones of the fire at the times shown; contours of the boundary temperature at $T = 400$ K for (a) the case U6u1L48o, that is outward ignition, and (b) U6u1L48i, inward ignition.

Finally, four ignition line lengths were considered: $L_i = 12$, 24, 48, 96 m. In these simulations the wind speed and ignition speed were held constant at $U_2 = 6$ m s^{-1} and $u_i = 1.0$ m s^{-1}, respectively. The largest ignition line length was chosen to better reflect the recommendations of Cheney and Gould (1995) who suggest that an ignition line length of 100 m or more is required for a fire to reach a quasi-equilibrium rate of spread. The $L_i = 48$ m matches the simulations of Moinuddin *et al.* (2018); Mell *et al.* (2007). The smaller ignition lengths were chosen to be commensurate with more modern experimental protocols; for example, Cruz *et al.* (2015b).

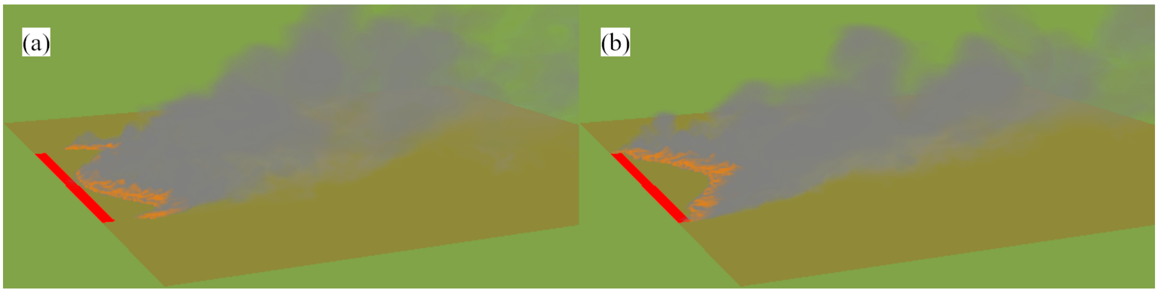

Figure 3: The fire fronts at 21 s after the ignition process commences rendered using Smokeview (Forney, 2019). The flame is visualised with the 80 kW m^{-3} isosurface of heat release rate per unit volume and the smoke is visualised with the soot mass fraction. (a) U6u1L48i (b) U6u1L48o.

An infinite speed ignition, that is instantaneous ignition along the entire length of the upwind edge, was also simulated as a control. The infinite ignition speed simulation was conducted with the wind speed and ignition line length held constant at $U_2 = 6$ m s^{-1} and $L_i = 48$ m respectively.

The defining parameters for each experiment are listed in Table 1. Note that in the simulation names the first number denotes the driving wind speed, the second number the ignition speed, and the third number the ignition line length. The 'i' or 'o' at the end of the simulation name denotes whether the ignition protocol is inward or outward, respectively. For example, 'U3u1L48o' denotes the simulation where the driving wind speed is 3 m s^{-1}, the ignition speed is 1.0 m s^{-1}, the ignition line length is 48 m, and the ignition protocol is outwards. It is of interest to note that 'U6u1L48o' matches case C064 from the Annaburroo experiments (Cheney *et al.*, 1993), which has been considered previously by Moinuddin *et al.* (2018) and Mell *et al.* (2007). The U6u1L48o case is identical to the 6 m s^{-1}, vegetation height 0.21 m of Moinuddin *et al.* (2018). The U6u1L48o case, is similar but not identical to the C064 case studied by Mell *et al.* (2007). The values of soot yield, the vegetation char fraction, vegetation element density, and vegetation heat of pyrolysis used here were also different to the values used by Mell *et al.* (2007). Mell *et al.* (2007) observed more spread on the lateral edges of the fire, than was observed by Moinuddin *et al.* (2018). Moinuddin *et al.* (2018) obtained results which were in better agreement with the experimental data of Cheney *et al.* (1993). The simulations of Mell *et al.* (2007) were conducted with 1 m resolution, compared to 0.25 m resolution used here. The finer grid resolution is likely the reason for the slower lateral spread of the fire.

Simulation	U_2 (m s^{-1})	u_i (m s^{-1})	L_i (m)
U3u1L48i, U3u1L48o	3	1.0	48
U6u1L48i, U6u1L48o	6	1.0	48
U6uInfL48	6	∞	48
U10u1L48i, U10u1L48o	10	1.0	48
U6u0.5L48i, U6u0.5L48o	6	0.5	48
U6u2.4L48i, U6u2.4L48o	6	2.4	48
U6u1L12i, U6u1L12o	6	1.0	12
U6u1L24i, U6u1L24o	6	1.0	24
U6u1L96i, U6u1L96o	6	1.0	96

Table 1: Simulation cases and defining parameter values.

Wind field development and its effect on fire spread

The simulated driving wind field should seek to replicate an atmospheric surface layer as closely as practicable and it is desirable that turbulent fluctuations in the simulations are statistically stationary. Experimental fires may experience strong gusts, i.e. large departures from the mean velocity that persist for significant times, leading to changes in the rate of spread, or the direction of the fire. In these simulations the mean profile is determined by the imposed inlet profile, equation (1), which is held constant in time. The flow is allowed to develop naturally through the domain. Because the inlet and initial conditions are kept constant for the inward and corresponding outward ignition protocol simulations, the wind field is largely controlled in these simulations. Moinuddin *et al.* (2018) demonstrate that after approximately $\tau = 4$ domain turnover times ($\tau = L_D/U_2$) that the flow develops to a log-law profile over the burnable area. The profile that develops over the simulated grassland is not the same as a log-law over a rough surface. The grass is modelled as a region of aerodynamic drag, so there is a shear-layer present above the grassland similar to the shear-layer above a tree canopy (Belcher *et al.*, 2012). Following Bou-Zeid *et al.* (2004) we fitted a log-law of the form

$$u(z) = \frac{u_*}{\kappa} \log\left(\frac{z}{z_0}\right), \tag{2}$$

where $\kappa = 0.4$ is von Karman's constant, u_* is the friction velocity, and z_0 is the equivalent roughness length. The equivalent roughness length characterises the canopy shear layer as a shift in the log region of the mean velocity profile. Because z_0 captures a shear layer, the measured value of z_0 will therefore be a function of the grass land properties (height, drag coefficient, leaf-area density) and z_0 will also depend on the driving velocity. Figure 4(a) shows the measured profiles and logarithmic fit for the three driving velocities ($U_2 = 3$, 6, and 10 m s^{-1}).

Moinuddin *et al.* (2018) compare the time series of $u-$velocity at $x = 405$ m, $y = \pm 50$ m, $z = 2$ m (the upstream corners of the burnable plot) to anemometer measurements from the Annaburoo grassfire experiments Cheney *et al.* (1993). The simulated time series of velocity matches the mean of that reported by Cheney *et al.* (1993), however, larger gusts are recorded in the experimental data. While the mean values match the experimental observations, the mean $u-$velocity at $x = 405$ m, $y = \pm 50$ m, $z = 2$ m is lower than the prescribed inlet velocity. The time series of the $u-$velocity at $x = 405$ m, $y = \pm 50$ m, $z = 2$ m for $U_2 = 3$, 6 and 10 m s^{-1} are shown in Figure 4(b). The $u(405, 50, 2, t)$ for all cases fluctuate around their mean values and therefore the wind fields are well developed.

To confirm that the turbulent fluctuations do not significantly effect the smoothed R results (details of the measurement and smoothing of R follow in the next section) a repeated simulation was performed where the ignition was delayed. Note that if the simulation is re-run without alteration, the same results will occur because the fire is subjected to exactly the same atmospheric flow; the initial wind conditions require some perturbation. By delaying the ignition time the fire will experience different turbulent fluctuations. However, because the turbulent fluctuations are statistically stationary, the $R(t)$ of the two simulations should be largely unaffected except for different fluctuations in R. The ignition was delayed by 100 s, which is comparable to the domain turnover time ($\tau = L_D/U_2 = 960/6 = 160$ s) for the simulation. The $R(t)$ for the two cases is shown in Figure 4(c). The difference in R is minor, and within the error bars estimated from the smoothing of the R data, which represent an uncertainty of approximately 10%; it is sufficient to use only a single simulation to obtain reliable results with a quantifiable error.

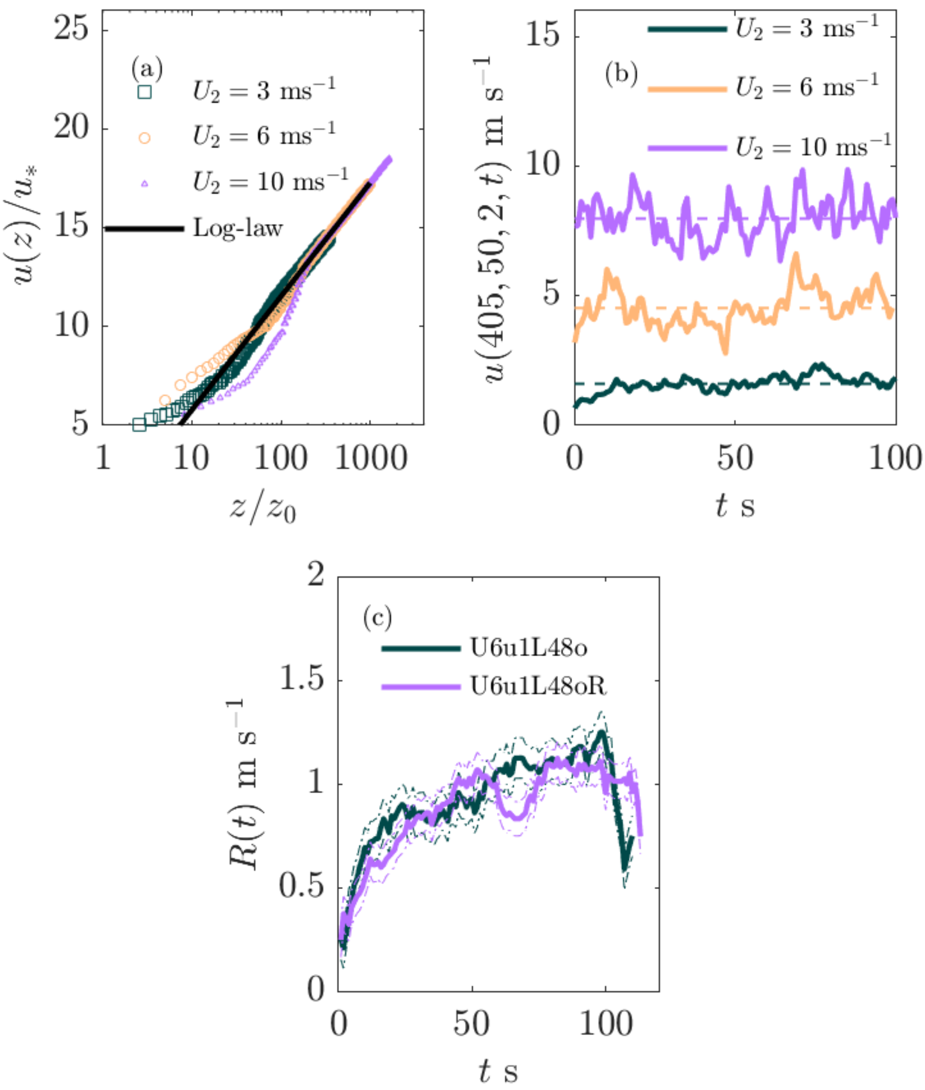

Figure 4: (a) velocity profiles over the fire plot for $u_2 = 3,\ 6,$ and 10 ms^{-1} and the fitted log-law profile. (b) Time series of $u(405, 50, 2)$ for $u_2 = 3,\ 6,$ and 10 ms^{-1}, the dashed lines are the time average of the velocity time series. (c) Variation in R for two runs of U6u1L48o

Centreline rate of spread development

Because the fire is symmetric it is sensible to examine only the geometric centreline of the fire. At each simulation output time (every 0.5 s) the temperature was extracted along the centreline of the fire. The head fire was associated with the largest peak in boundary temperature. The fire centre location was identified as $x_*(t) = ((x_1 - x_0))/2 + x_0$, where x_0 and x_1 are the left and right x-locations of where the peak exceeds $T = 400$ K. This definition is analogous to that used by Apte *et al.* (1991).

The standard first-order forward finite difference was used to obtain the approximate $R(t)$ over time. The $R(t)$ data were smoothed using a 10 point moving average to reduce noise caused by turbulent fluctuations. The variance between the smoothed and raw data was used as measure of uncertainty in $R(t)$. Plotting R as a function of x_* allows assessment of variation in the initial location of the head fire and allows the minimum size of a burn plot required to allow development of a quasi-equilibrium state to be quickly identified.

An alternative means of obtaining an averaged, quasi-equilibrium rate of spread, R_{qe}, is to use least-squares regression to fit a straight line to the fire centre location $x_*(t)$ over the region where the fire spread appears linear. The average R_{qe} is then the slope of the fitted line. The region where the fire front is advancing at a constant rate can be subjective to identify. We simply picked the largest time interval where the $R(t)$ appeared to be constant; choosing other slightly different time intervals made very little difference to the R_{qe}. The goodness of fit statistic r^2 between a straight line with slope R_{qe} and the fire front location $x_*(t)$ was always above 0.9.

Firstly, we examined R for fixed ignition line length, ignition speed, and wind speed; the only variation is the direction of the ignition line. The R values for U6u1L48i and U6u1L48o are plotted in Figure 5. In this figure, R is plotted against time in panel (a), and against fire distance along the plot in panel (b). Because the inward ignition protocol takes approximately 30 s before a centreline fire is established, R is apparently shifted forward for the U6u1L48i case in figure 5(a). The reason for the lag in centreline R is clear from Figure 2, the fire exhibited a pronounced v-shape as a result of the ignition protocol. The fire front then surged forward leading to the inward ignition fire propagating faster than the outward ignition fire. Rate of spread values $R(t)$ are shown as thick solid lines, while the uncertainties in the simulation results are depicted using thin dashed lines of the same colour. The uncertainties were taken as the smoothed rate-of-spread time series plus or minus the variance of the non-smooth rate-of-spread time series. The uncertainties in R are about 10% of the corresponding rate of spread values. In subsequent plots, we will omit the uncertainty lines.

The fires both achieved approximately the same quasi-equilibrium rate of spread, $R_{qe} \approx$ 1.1 m s^{-1}, at approximately 60 s and 50 s after ignition for the inward and outward protocols, respectively. For both cases this corresponds to 50 m downstream of the ignition line. The R for the inward ignition protocol fluctuated greatly: between 25 s and 60 s (or 0 to 50 m), with R peaking at approximately 1.7 m s^{-1}. The peak in R has been discussed by Viegas *et al.* (2012) for merging junction fires. In essence, the inward protocol is similar to two straight-line fires merging at a V-shaped junction. The acceleration phase should be enhanced as the ignition line speed decreases, and the fire front closer approximates a V-shaped junction fire. In contrast, R for the the outward ignition protocol grew steadily to the quasi-equilibrium value R_{qe}. The initially high rate of spread in the inward ignition case lead to an overall faster moving fire: the inward ignition protocol reached the end of the plot a approximately 80 s after ignition and the outwards ignition protocol reached the end of the plot at approximately 110 s after ignition.

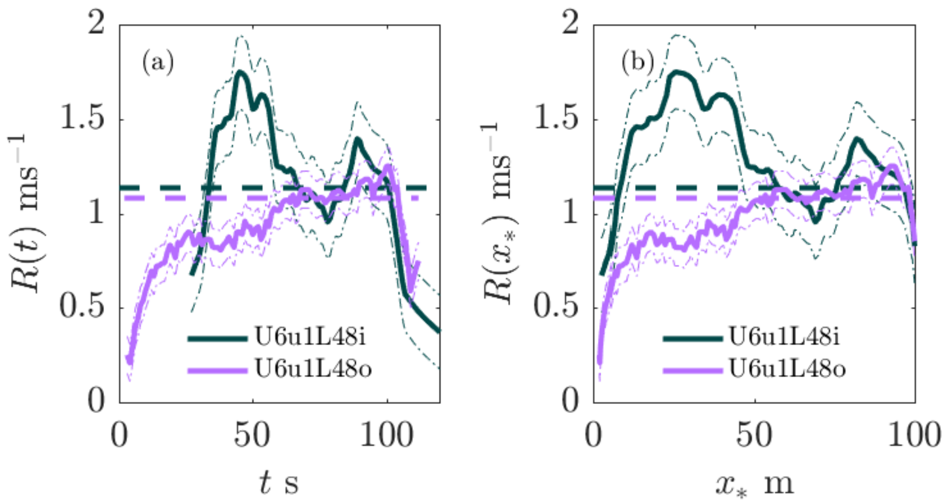

Figure 5: Variation in R for U6u1L48i and U6u1L48o. (a) R is plotted versus time, (b) R is plotted versus fire front location x_*. The thin broken lines are the uncertainties in R estimated from the variance of the data. The thick dashed lines are computed from a linear regression fit to the fire front location x_* in the quasi-equilibrium region.

The rate of spread as wind speed was varied is shown in Figure 6. The result for the inward ignition protocol for $U_2 = 10$ m s^{-1} was similar to the $U_2 = 6$ m s^{-1} case. Rate of spread increased for $x_* < 30$ m and then decreased to a quasi-equilibrium value of $R_{qe} \approx 1.5$ m s^{-1} at approximately $x_* = 60$ m. However, R for the $U = 3$ m s^{-1} (inward ignition) case quickly rose to the quasi-equilibrium value at $R_{qe} = 0.9$ m s^{-1}. The outwards ignition cases all rose steadily to the quasi-equilibrium values.

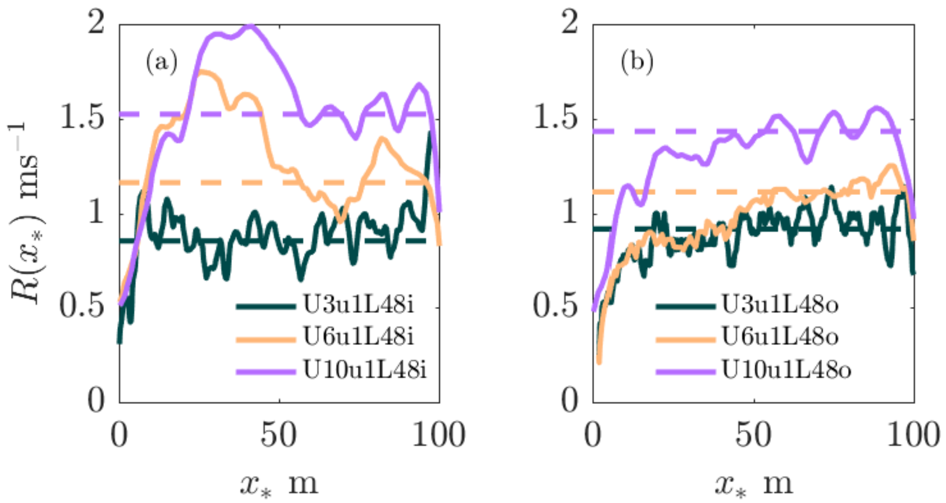

Figure 6: Effect of inlet 2 m wind speed upon R for inward ignition (a) and outward ignition (b). The quasi-equilibrium R_{qe} increases with wind speed. The surge behaviour is visible in the U10u1L48i case but not the U3u1L48i case nor any of the outward-ignition cases.

The effect of ignition line length upon R is shown in Figure 7. The U6u1L96i case was aberrant: no quasi-equilibrium was reached and the fire exhibits an acceleration and deceleration phase like a merging junction fire (Raposo *et al.*, 2018), rather than the development to a quasi-equilibrium R like the line fires of Cheney *et al.* (1993) and Cruz *et al.* (2015b). If the U6u1L96i case is considered in isolation, the central part ($40 < x < 60$ m) may be thought to be at a quasi-equilibrium R, especially on a relatively short burn plot. The trend for the shorter ignition length cases, however, suggests this is a transient peak in R, and that U6u1L96i does not achieve a quasi-equilibrium R. For all other cases, there was a slight increase in quasi-equilibrium R_{qe} as the ignition line increases, however, this trend was neither large nor significant. For the inward ignition cases (except U6u1L96i): for the $L_i = 12$ m case $R_{qe} \approx 0.94$ m s^{-1} in the quasi-equilibrium regime; for the $L_i = 48$ m case $R_{qe} \approx= 1.16$ m s^{-1}. The uncertainty in R is 0.1 m s^{-1} so the observed differences are close to the noise level. It should be noted that the difference in R_{qe} at different ignition lengths is about 25%. Canfield *et al.* (2014) observed that ignition line length does effect the overall R_{qe}, however, their study considered ignition line lengths of up to 400 m. The outward ignition cases also showed an increasing trend with increasing L_i but the magnitude of the increase was small. The U6u1L96o case exhibited greater fluctuations than the other cases with a lower ignition line length. However, the R_{qe} for the U6u1L96o case is only approximately 5% higher than for the U6u1L48o case. Cheney and Gould (1995) suggested that an ignition line of greater than 100 m length is required to achieve a fire that reaches the quasi-equilibrium spread regime. With the exception of the U6u1L96i case, the simulation results suggest that L_i does not greatly effect R_{qe}, but L_i does effect the variation in $R(t)$ (or equivalently $R(x_*)$). The U6u1L96i case suggests that the inwards ignition protocol is unsuitable for experimental fires of this size, where the experiment aims to study line fires. More research is required to completely understand how fire development depends on the initial size of the fire.

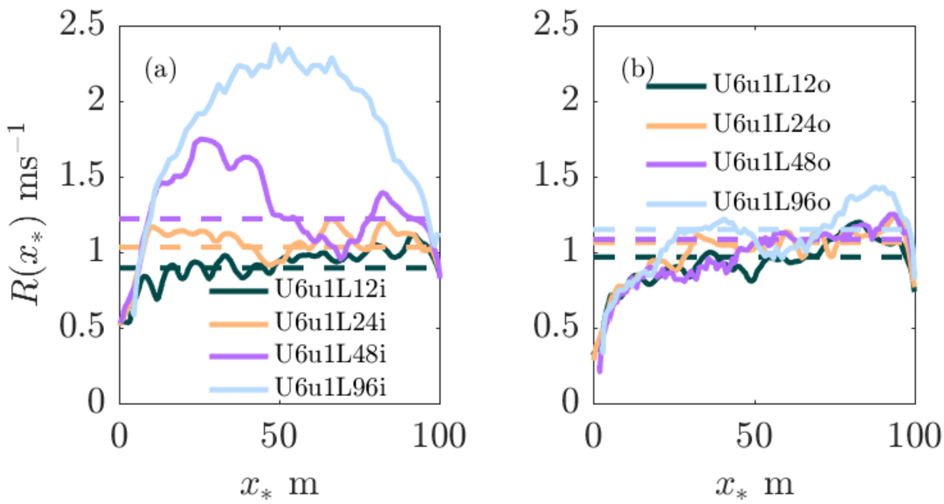

Figure 7: Variation of R with varying ignition line length. The U6u1L96i case is aberrant (see text). For the other cases, some increase in quasi-equilibrium R_{qe} is observed with increasing ignition line length in the inward ignition cases (a), but not with the outwards ignition cases (b).

The effect of varying the ignition speed on R is shown in Figure 8. For these simulation cases, the time taken for the ignition to progress from the starting point to the end point was changed to give the stated ignition speed. Interestingly, the rate of spread of the outward ignition protocol was not significantly affected by increasing the ignition speed, however, for the inward ignition R was greatly affected. The faster ignition speed, 2.4 m s^{-1}, achieved a quasi-equilibrium within approximately 20 m. The slower ignition speed, 0.5 m s^{-1} did not achieve a quasi-equilibrium rate of spread. Due to the slow ignition speed, two distinct parabolic shaped fires developed and then merged together as the ignition reached the middle of the plot. The R_{qe} achieved using the outward ignition protocol seems largely unaffected by ignition line speed. Figure 7(b) shows that the three simulations appear to give convergent results for $R(x_*)$. Perhaps this is because the head fire is established immediately at ignition and the head fire grows slowly as the flanks of the fire develop with subsequent ignition.

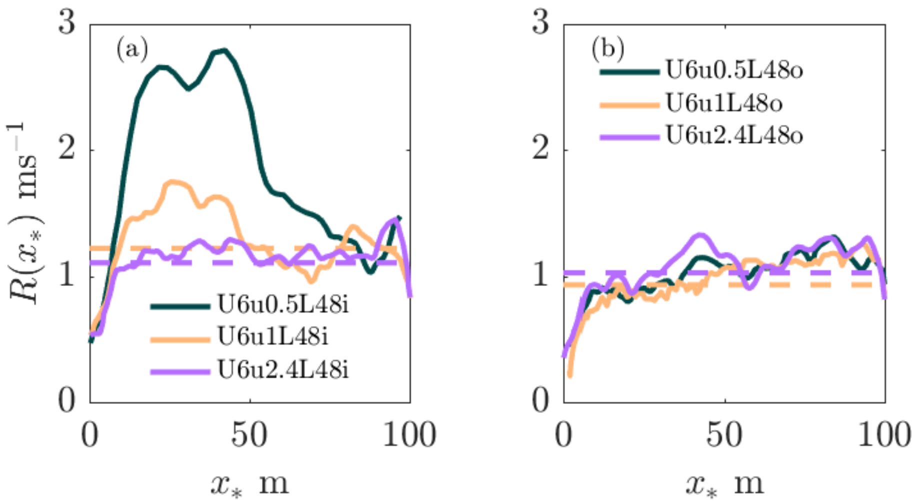

Figure 8: The effect of ignition line speed on R. The inward protocol (a) showed that a faster ignition line speed yields quasi-equilibrium R_{qe} quickly, whereas a slow ignition line speed led to a large surge in R and no overall quasi-equilibrium state. The outwards ignition protocols were unaffected by ignition line speeds (b).

Figure 9 compares the U6u1L48i and U6u1L48o cases to an infinite ignition speed simulation (U6uInfL48), in which all 48 m of the initial fire line was ignited simultaneously. The U6uInfL48 case can be seen as an ignition protocol control simulation representing the limiting cases of both ignition protocols. This could possibly be realised in experiments by a line of accelerant ignited automatically at many points along the line. The U6uInfL48 simulation reached a quasi-equilibrium state, at approximately 35 m, which is earlier than the inward and outward protocol simulations for the same wind speed and ignition line length. The U6uInfL48 case also did not exhibit the initial surge observed in the U6u1L48i case.

Interestingly, between about $x_* = 10$ m and $x_* = 30$ m, the U6uInfL48 case exhibited a quasi-steady rate of spread that was slightly-lower than the value of R_{qe} attained in the later stages of development.

The difference between the smoothed R and the quasi-equilibrium R_{qe} was within the uncertainty level in R (approximately 10%), as measured by the variance of R over the whole simulation time. Overall, faster ignition speed gives an initial fire line which is closer to a straight line and the overall development is more uniform relative to both the inward and outwards ignition protocol cases.

In this investigation of the effects of ignition line length and ignition line speed, full factorial experimental design was not considered. Instead the ignition speed was fixed at a single value 1 ms^{-1} and L_i varied; or L_i was fixed at 48 m and u_i was varied. This choice reflects the contemporary experimental protocols used in Cheney *et al.* (1993), Cheney *et al.* (1998), and Cruz *et al.* (2015b). If L_i varies with constant u_i then the time for the ignition to be completed varies and could impact $R(t)$. Because we seek to assess realistic experimental protocols, our choice of varying L_i for a single fixed u_i (and vice versa) will not affect our conclusions. It may be of interest to investigate the effect of ignition time on $R(t)$ in a future study.

Two-dimensional rate of spread development

The normal velocity of the two-dimensional front was obtained through a curve-fitting and extrapolation algorithm. Once the fire established itself as a single continuous fire line, the centre of the pyrolysis region was obtained for each $y-$point and each time step; that is, $x_*(y_j, t_n)$. A sixth-order polynomial, $p_n(y)$, was fitted to the $x_*(y_j, t_n)$ points. This process was repeated until the fire impinges upon the end of the burning plot. The

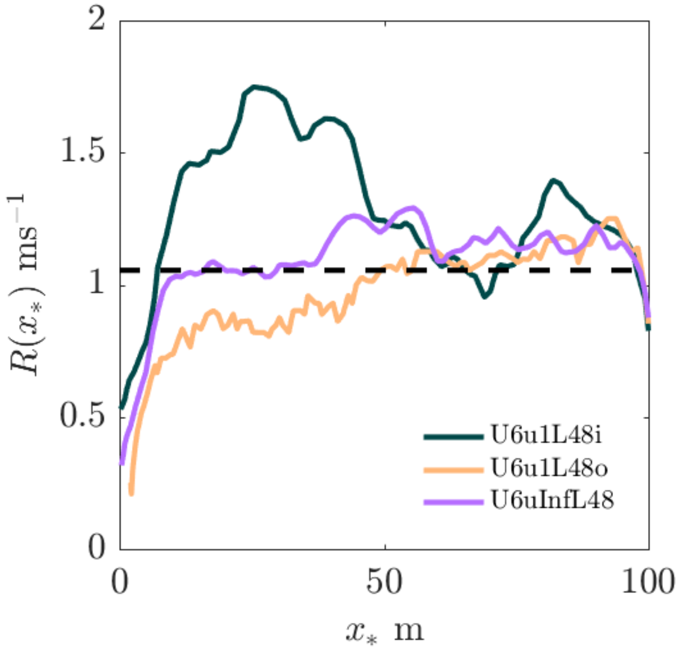

Figure 9: Comparison of the R for U6u1L48i, U6u1L48o, and U6uInfL48, the infinitely fast ignition line simulation.

goodness of the polynomial fit is assessed by Pearson's r^2 value; r^2 is always greater than 0.9 indicating that the sixth-order polynomial fit is adequate. The next part of the algorithm estimates the normal velocity of the curve by measuring the distance between $p_n(y_j)$ and $p_{n+1}(y)$ along the line normal to $p_n(y_j)$. Because the time between outputs $\delta t = t_{n+1} - t_n$ is known, the normal velocity of the curve $p_n(y)$ can be approximated. For every y_j we compute the line normal to $p_n(y)$ at y_j; the line is denoted $l_{j,n}(y)$. The equation of the line is

$$l_{j,n}(y) = p_n(y_j) - \left(\frac{dp_n}{dy}(y_j)\right)^{-1}(y - y_j)\,. \tag{3}$$

The point of intersection, y_*, between the $l_{j,n}(y)$ is found by solving

$$p_{n+1}(y_*) - l_{j,n}(y_*) = 0\,, \tag{4}$$

numerically using the Newton-Raphson scheme. The normal velocity at y_j is then

$$u_n(y_j) = \frac{((l_{j,n}(y_*) - p_n(y_j))^2 + (y_* - y_j)^2)^{1/2}}{\delta t}\,. \tag{5}$$

The resulting normal velocity is visualised as a function of y and t. The shaded surfaces of u_n for U6u1L48i and U6u1L48o are shown in Figure 10. There is minor noise in these plots, however, additional smoothing as was used. The polynomial fit to the centre of the pyrolysis region tends to much of the noise in the u_n data.

In Figure 10 the inward ignition protocol starts later than the outward ignition protocol; this is because u_n was computed from the instant a single connected fire line exists. As shown in Figure 2 the inward ignition protocol was overall much faster to burn to the end of the plot. To remove difficulties with fitting the polynomial to disconnected regions, the u_n calculation is stopped before the fires reach the end of the burnable plot.

The colouring in Figure 10 separates head fire motion (fast, yellow) from flank fire motion (slow, blue). The figure illustrates the growth in overall fire line width, which occurs in two phases. At approximately 50 s the fire line increased in width, however, the edges have low u_n-velocity so this increase corresponded to a thickening of the flanks of the fire. Some increase in the head fire width was apparent but this was minor; for both cases the head fire appears fairly well constrained to the range $-20 < y < 20$ m. The emergence of the quasi-equilibrium state is also apparent in these surface plots.

The speed u_n appeared to equilibrate after approximately 70 s for both the inward ignition protocol and outwards ignition protocol. For the outwards ignition protocol, however, more simulation time is required to make this conclusion definitive. The most prominent feature was the large local maximum of u_n for the inward ignition case. This maximum shows the centre of the fire rushing forwards from approximately $t = 40$ s to $t = 60$ s. This is consistent with the centreline velocity shown in Figure 5(a). Comparing the spatial velocity pattern in Figure 10(b) with the development of the fire depicted in Figure 2(b) reveals that the region of maximum u_n corresponds to the stage of fire development in which the fireline exhibited a region of negative curvature. The increased velocity is localised to the region of negatively curved fire line, which accelerated forward. The rate of spread decreased back to the quasi-equilibrium R_{qe} once the fireline had achieved its final, roughly parabolic, shape. This localised increase in the rate of spread is consistent with the observations of Hilton *et al.* (2017) and Hilton *et al.* (2018). Hilton *et al.* (2018) demonstrated that the acceleration in the fireline is a convective effect. The fire produces a buoyancy-driven flow which is enhanced in regions of negative curvature, in turn leading to acceleration of the fire.

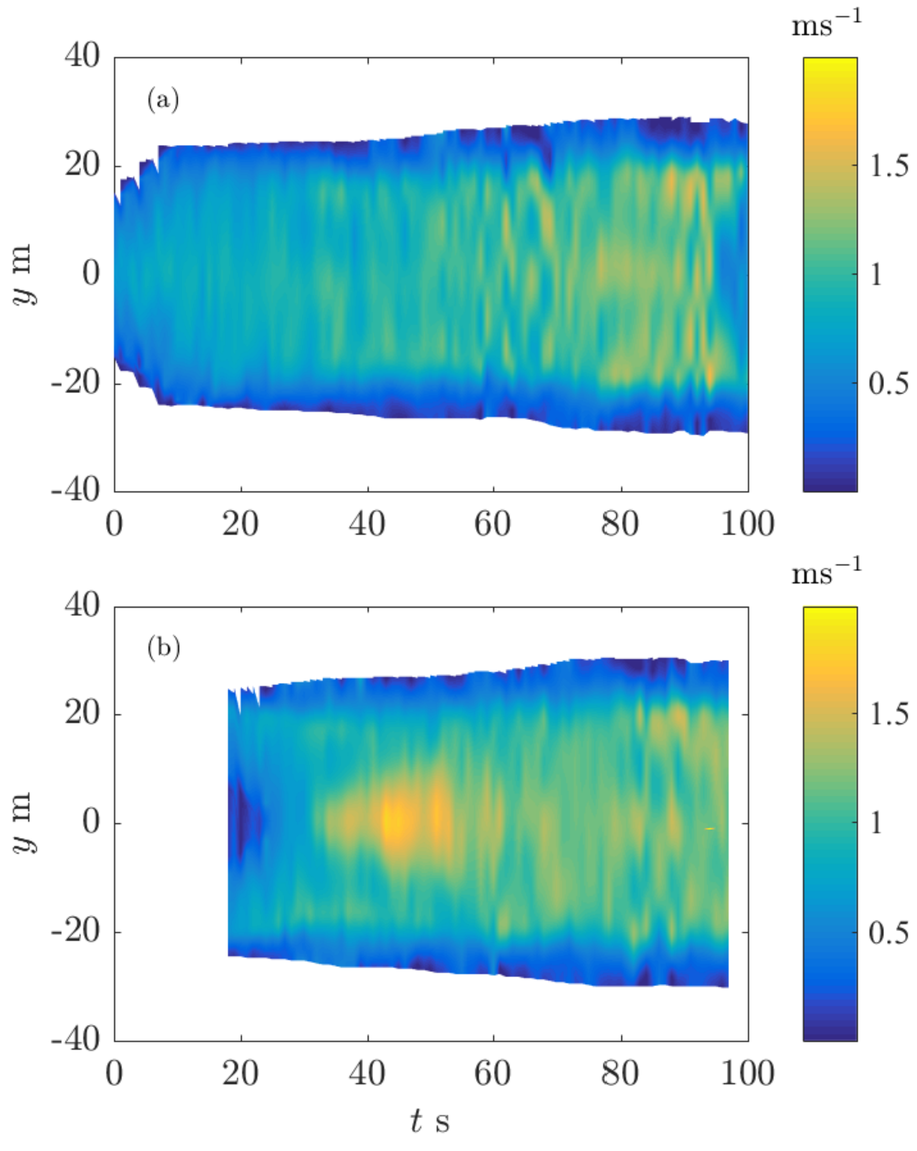

Figure 10: The speed of the fire front as a function of time and y-distance. (a) Outwards ignition (b) inward ignition.

Convective number development

Recently, Morvan and Frangieh (2018) attempted to clarify the use of dimensionless parameters to characterise fire behaviour as wind-driven or buoyancy-driven fires.

Morvan and Frangieh (2018) characterised fires using the Byram number:

$$N_c = \frac{2gQ}{(U_{10} - R)^3 \rho c_p T_a} \,. \tag{6}$$

Here U_{10} is a velocity scale far from the flame, taken here as the time averaged velocity at the fire ground at 10 m, i.e. $\overline{u}(405, 50, 10)$. The unitless factor of two acts only as a scaling and contributes no information; we retain it only for consistency with the literature. The other parameters used to compute N_c were the ambient temperature in the simulation $T_a = 305$ K, the density $\rho = 1.2$ kg m^{-3} and specific heat of air $c_p = 1.0$ kJ kg^{-1} K^{-1}.

Morvan and Frangieh (2018) provided bounds on N_c to classify a fire as wind-driven or buoyancy-driven. Using data from wildfires and experimental fires Morvan and Frangieh determined that if $N_c > 10$ the fire is buoyancy-driven, and if $N_c < 2$ the fire is wind-driven – this is consistent with $\mathcal{O}(N_c) = 1$ for transition between the two modes. At intermediate N_c values the fire is neither buoyancy-driven nor wind-driven. It is hypothesised that an intermediate regime, called the surge-stall regime Dold and Zinoviev (2009); Dold (2010), occurs in the intermediate range of N_c where the fire oscillates between the wind-driven and buoyancy-driven modes.

Intensity at each time step Q_n was computed as the globally averaged heat release rate, divided by the fire line length measured along the centre of the pyrolysis region at each time step. The fire line length was determined using the arc length of the polynomial fit, $p_n(y)$, to the centre of the pyrolysis region. That is

$$Q = \frac{\langle HRR \rangle}{\displaystyle\int_{y_i}^{y_f} \left(1 + \left(\frac{dp_n}{dy}\right)^2\right)^{1/2} dy} \,. \tag{7}$$

Note that the integral was computed from the first burning $y-$location, y_i to the final burning $y-$location, y_f. Using mid-flame measurements of wind as the relevant velocity scale could be more appropriate; however it seems that the choice of best wind scale in the Byram number is still an open problem. Using mid-flame measurements would change the N_c values computed here.

The simulated N_c for all cases is shown in Figure 11. There is an increase in N_c for $x_* < 50$ m for the inward ignition cases (shown in Figure 11(a) and Figure 11(c)), however with the exception of the U6u0.5L48i and U6Lu1L96i cases, the fires are still within the wind driven regime. The N_c for the U6u0.5L48i and U6Lu1L96i cases indicates that the initial surge of these fires are transitional and possibly within the so-called surge-stall regime (Dold and Zinoviev, 2009; Dold, 2010). Greater insight into fires with $2 < N_c < 10$ is required to understand and completely classify fires in the surge-stall regime.

The two lowest wind speed cases (shown in Figure 11(b)) are classified as buoyancy dominated given the large N_c. Note the large value of N_c is consistent with observations for grass fires of Morvan and Frangieh (2018).

The application of dimensional analysis to characterise fire behaviour simulated here would also be of interest. Provided that dimensionless parameters are used, the resulting characterisation of fires should be equivalent, regardless of the individual scales chosen. Such analysis would allow more general models of fire spread to be constructed, however, such a study is beyond the scope of the present work.

Conclusions

The simulation results demonstrate that the ignition protocol effects the development of a fire to its quasi-equilibrium rate of spread. The ignition protocol may then effect statistical analysis of experimental results, however, it is not known which, if any, historic experimental results will be adversely affected. It is possible that, particularly for inward ignition cases with a large initial acceleration of the fire, experimental fires could have

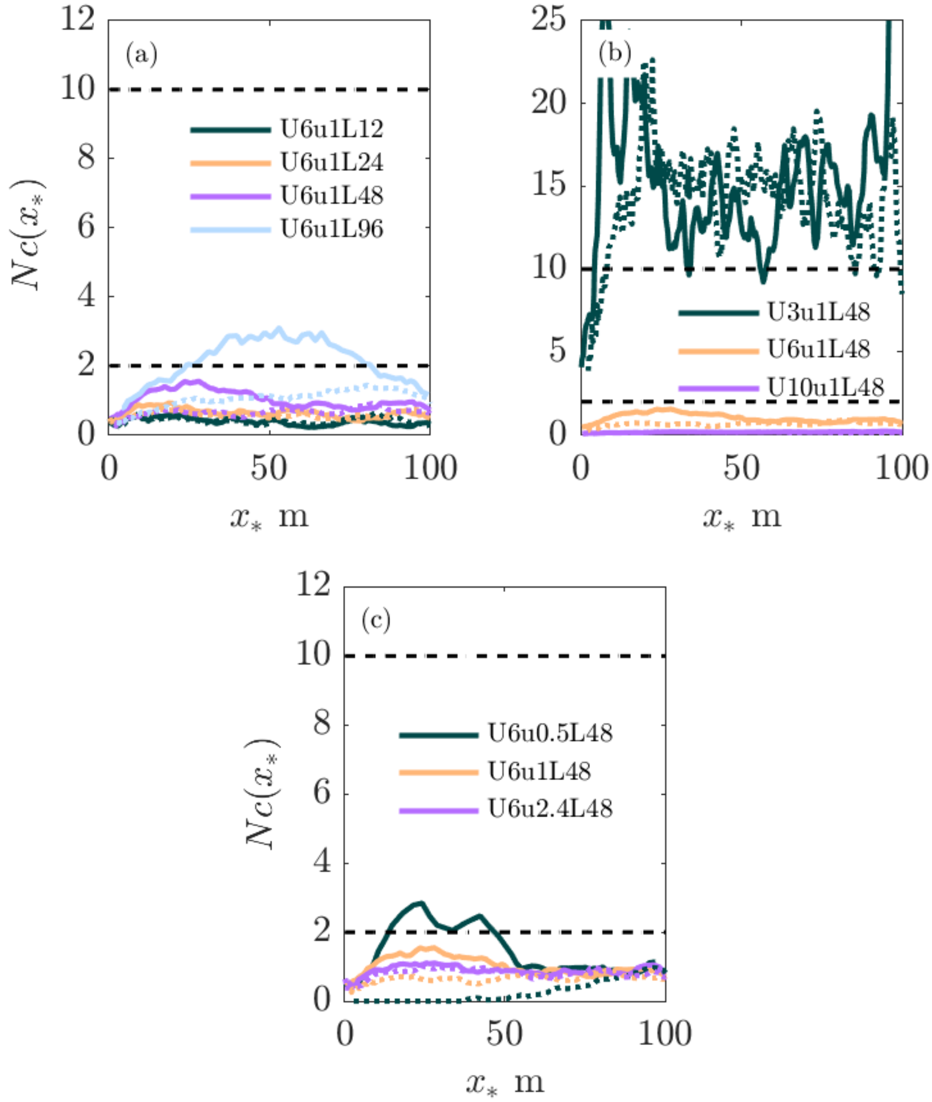

Figure 11: Byram numbers for all cases. (a) Variation in ignition line length, (b) variation of wind speed (c) variation in ignition speed. The solid line represents the inward ignition protocol and the dashed line is the outward protocol.

been measured in a surge-stall regime which may leaded to overestimated R_{qe}. The simulated fires typically develop to a quasi-equilibrium rate of spread in approximately 50 m (over a 100 m) plot, consistent with Cruz *et al.* (2015b) who observed that the fire took approximately half of the plot length to develop to a quasi-equilibrium spread rate. However, Cruz *et al.* (2015b) made this observation on much smaller burn plots (33 m on each side). We observed that the ignition line length in the inward ignition cases appeared to influence the development to a quasi-equilibrium R_{qe}, however, we did not test the effect of a narrower burnable plot.

Experimental fires are often complicated by variable wind fields, non-homogeneous fuels, and rough terrain. Therefore, researchers must be cautious when using the results of simulation studies to inform experimental practice. However, the simulated inward ignition protocol $R(x_*)$ results are overwhelming: using the inward ignition protocol with a modest to slow ignition line speed in typical wind conditions yields a fire that surges forward rather than developing monotonically to a quasi-equilibrium rate of spread. Experimentalists should seek to establish a quasi-equilibrium rate of spread as quickly as possible and ensure that experimental plots are of sufficient length so that (a) the fire does indeed achieve a quasi-equilibrium state, and (b) the fire does not undergo unintended surging behaviour, or the surging behaviour has subsided before data is sampled. Therefore, the simulation results suggest that the inward ignition protocol should not be used. The outward ignition protocol does not produce oscillations and overall may be a more prudent choice. If available, an automatic ignition line that gives an effectively infinite ignition line speed appears preferable.

Given the emergence of drone technology and high speed videography, it is possible to accurately record the position of an experimental fire at high temporal resolution. Sullivan *et al.* (2018) have studied the development of fires from a point ignition using drone footage and were able to measure the development in the rate of spread. Measuring R as a function of time (or distance) is a valuable experimental endeavour. Such information would facilitate additional validation for physics-based simulations, but would also support refined statistical analyses of the experimental results. Collecting such detailed information over a range of wind speeds, and complementing experimental analyses with further numerical simulations, could also provide additional insights into the surge-stall regime.

Acknowledgements

This research was supported by the Bushfire and Natural Hazards Cooperative Research Centre and some computational resources were provided by the University of Melbourne

Research Platforms. This research was also undertaken with the assistance of resources and services from the National Computational Infrastructure (NCI), which is supported by the Australian Government.

Conflicts of Interest

The authors declare no conflicts of interest.

Nomenclature

t	s	time
x, y	m	streamwise and lateral coordinates, respectively
t_n	s	the time at the n^{th} time step
y_j	m	the j^{th} grid point in the $y-$direction
y_i, y_f	m	minimum and maximum $y-$locations that are burning at a particular time step
U_2	m s^{-1}	the inlet wind speed, specified at 2 m above the ground
U_{10}	m s^{-1}	velocity scale for the Byram number; taken as the $u-$velocity at 10 m from the ground over the burnable plot
u, v, w	m s^{-1}	fluid velocities, a prime ($'$) denotes the fluctuation from the mean
L_i	m	Ignition line length
L_D	m	Domain length
u_i	m	Ignition line speed
l	m	descretised ignition line segment $l = L_i/8$
δt	s	simulation time step
δt_i	s	descretised ignition time step $\delta t_i = l/u_i$
x_0 and x_1	m	trailing and leading edges of the pyrolysis region along $y = 0$ respectively.
x_*	m	fire location on the centreline. The mid-point between x_0 and x_1, strictly a function of time.
$x*(y_j, t_n)$	m	fire location in the lateral grid point y_j, at time step t_n.
R	m s^{-1}	Rate of spread
$R(t)$ $R(x_*)$	m s^{-1}	R as a function of time or distance from the ignition
R_{qe}	m s^{-1}	Quasi-equilibrium rate of spread
τ	s	domain turnover timescale, i.e. the length of the domain divided by a characteristic velocity
r^2		goodness of fit statistic.
$p_n(y)$		a 6^{th} order polynomial fitted to the fire line at time step t_n
$l_{j,n}(y)$		a line starting at y_j at time step t_n used in the calculation of the normal velocity of the fire line
y_*	m	point of intersection between the construction line $l_{j,n}(y)$ and the fire line $p_{n+1}(y)$ at the subsequent time step
$u_n(y_j)$	m s^{-1}	the normal velocity of the fire line at lateral location y_j and time step t_n
u_n	m s^{-1}	the normal velocity of the fire line, a function of time and $y-$location
N_c		Byram number
$T_a = 305$	K	ambient temperature
$\rho = 1.2$	kg m^{-3}	denisty of air
$c_p = 1.0$	kJ kg^{-1} K^{-1}	specific heat of air .
$g = 9.8$	m s^{-2}	gravitational acceleration
Q	kW m^{-1}	fire intensity.
HRR	kW	Heat release rate

References

Apte, VB, Bilger, RW, Green, AR, and Quintiere, JG (1991) Wind-aided turbulent flame spread and burning over large-scale horizontal PMMA surfaces. *Combustion and Flame* **85**, 169–184. doi:10.1016/0010-2180(91)90185-E.

Belcher, SE, Harman, IN, and Finnigan, JJ (2012) The wind in the willows: flows in forest canopies in complex terrain. *Annual Review of Fluid Mechanics* **44**, 479–504. doi:10.1146/annurev-fluid-120710-101036.

Bou-Zeid, E, Meneveau, C, and Parlange, MB (2004) Large-eddy simulation of neutral atmospheric boundary layer flow over heterogeneous surfaces: Blending height and effective surface roughness. *Water Resources Research* **40**. doi:10.1029/2003WR002475.

Canfield, JM, Linn, RR, Sauer, JA, Finney, M, and Forthofer, J (2014) A numerical investigation of the interplay between fireline length, geometry, and rate of spread. *Agricultural and Forest Meteorology* **189**, 48–59. doi:10.1016/j.agrformet.2014.01.007.

Cheney, NP and Gould, JS (1995) Fire growth in grassland fuels. *International Journal of Wildland Fire* **5**, 237–247. 10.1071/WF9950237.

Cheney, NP, Gould, JS, and Catchpole, WR (1993) The influence of fuel, weather and fire shape variables on fire-spread in grasslands. *International Journal of Wildland Fire* **3**, 31–44. doi:10.1071/WF9930031.

Cheney, NP, Gould, JS, and Catchpole, WR (1998) Prediction of fire spread in grasslands. *International Journal of Wildland Fire* **8**, 1–13. doi:10.1071/WF9980001.

Cruz, MG, Gould, JS, Alexander, ME, Sullivan, AL, McCaw, WL, and Matthews, S (2015a) A guide to rate of fire spread models for Australian vegetation. Australasian Fire and Emergency Service Authorities Council Limited and Commonwealth Scientific and Industrial Research Organisation.

Cruz, MG, Gould, JS, Kidnie, S, Bessell, R, Nichols, D, and Slijepcevic, A (2015b) Effects of curing on grassfires: II. effect of grass senescence on the rate of fire spread. *International Journal of Wildland Fire* **24**, 838–848. doi:10.1071/WF14146.

Dold, JW (2010) Vegetation engagement in unsteady fire spread. In 'Proceedings of the VI International Conference on Forest Fire Research', pages 15–18.

Dold, JW and Zinoviev, A (2009) Fire eruption through intensity and spread rate interaction mediated by flow attachment. *Combustion Theory and Modelling* **13**, 763–793. doi:10.1080/13647830902977570.

Forney, GP (2019) Smokeview, A Tool for Visualizing Fire Dynamics Simulation Data Volume I: Users Guide. US Department of Commerce, National Institute of Standards and Technology.

Frangieh, N, Morvan, D, Meradji, S, Accary, G, and Bessonov, O (2018) Numerical simulation of grassland fires behavior using an implicit physical multiphase model. *Fire Safety Journal* **102**, 37–47. doi:10.1016/j.firesaf.2018.06.004.

Hilton, JE, Miller, C, Sharples, JJ, and Sullivan, AL (2017) Curvature effects in the dynamic propagation of wildfires. *International Journal of Wildland Fire* **25**, 1238–1251. doi:10.1071/WF16070.

Hilton, JE, Sullivan, AL, Swedosh, W, Sharples, J, and Thomas, C (2018) Incorporating convective feedback in wildfire simulations using pyrogenic potential. *Environmental Modelling & Software* **107**, 12–24. doi:10.1016/j.envsoft.2018.05.009.

Linn, RR and Cunningham, P (2005) Numerical simulations of grass fires using a coupled atmosphere–fire model: basic fire behavior and dependence on wind speed. *Journal of Geophysical Research: Atmospheres* **110**, D13107. doi:10.1029/2004JD005597.

McDermott, R, McGrattan, KB, and Floyd, J (2011) A simple reaction time scale for under-resolved fire dynamics. *Fire Safety Science* **10**, 809–820. doi:10.3801/IAFSS.FSS.10-809.

McGrattan, K, Hostikka, S, Floyd, Jand Baum, HR, Rehm, RG, Mell, W, and McDermott, R (2013) Fire dynamics simulator (version 6), technical reference guide. *NIST special publication* **1018**.

Mell, W, Jenkins, MA, Gould, J, and Cheney, P (2007) A physics-based approach to modelling grassland fires. *International Journal of Wildland Fire* **16**, 1–22. `doi:10.1071/WF06002`.

Moinuddin, KAM, Sutherland, D, and Mell, W (2018) Simulation study of grass fire using a physics-based model: striving towards numerical rigour and the effect of grass height on the rate-of-spread. *International Journal of Wildland Fire* **27**, 800–814. `doi:10.1071/WF17126`.

Morvan, D and Dupuy, JL (2004) Modeling the propagation of a wildfire through a mediterranean shrub using a multiphase formulation. *Combustion and Flame* **138**, 199–210. `doi:10.1016/j.combustflame.2004.05.001`.

Morvan, D and Frangieh, N (2018) Wildland fires behaviour: wind effect versus byrams convective number and consequences upon the regime of propagation. *International Journal of Wildland Fire* **27**, 636–641. `doi:10.1071/WF18014`.

Morvan, D, Meradji, S, and Mell, W (2013) Interaction between head fire and backfire in grasslands. *Fire Safety Journal* **58**, 195–203. `doi:10.1016/j.firesaf.2013.01.027`.

Raposo, JR, Viegas, DX, Xie, X, Almeida, M, Figueiredo, AR, Porto, L, and Sharples, J (2018) Analysis of the physical processes associated with junction fires at laboratory and field scales. *International Journal of Wildland Fire* **27**, 52–68. `doi:10.1071/WF16173`.

Sullivan, AL, Cruz, MG, Hilton, JE, Plucinski, MP, and R., Hurley (2018) Study of growth of free-burning grass fires from point ignition. In 'Proceedings of the VIII International Conference on Forest Fire Research', pages 643–649.

Viegas, DX, Raposo, JR, Davim, DA, and Rossa, CG (2012) Study of the jump fire produced by the interaction of two oblique fire fronts. part 1. analytical model and validation with no-slope laboratory experiments. *International Journal of Wildland Fire* **21**, 843–856. doi:10.1071/WF10155.